Research in Astronomy and Astrophysics, 23:035010 (7pp), 2023 March https://doi.org/10.1088/1674-4527/acb9de

An Intermediate-field Fast Radio Burst Model and the Quasi-periodic Oscillation

Jie-Shuang Wang[1], Xinyu Li[2,3], Zigao Dai[4,5], and Xuefeng Wu[6]
[1] Max-Planck-Institut für Kernphysik, Saupfercheckweg 1, D-69117 Heidelberg, Germany; jswang@mpi-hd.mpg.de
[2] Canadian Institute for Theoretical Astrophysics, 60 St George St, Toronto, ON M5R 2M8, Canada
[3] Perimeter Institute for Theoretical Physics, 31 Caroline Street North, Waterloo, Ontario, N2L 2Y5, Canada
[4] Department of Astronomy, University of Science and Technology of China, Hefei 230026, China
[5] School of Astronomy and Space Science, Nanjing University, Nanjing 210023, China
[6] Purple Mountain Observatory, Chinese Academy of Sciences, Nanjing 210023, China
Received 2022 December 15; revised 2023 January 17; accepted 2023 January 30; published 2023 February 28

Abstract

Quasi-periodic oscillation (QPO) signals are discovered in some fast radio bursts (FRBs) such as FRB 20191221A, as well as in the X-ray burst associated with the galactic FRB from SGR 1935+2154. We revisit the intermediate-field FRB model where the radio waves are generated as fast-magnetosonic waves through magnetic reconnection near the light cylinder. The current sheet in the magnetar wind is compressed by a low frequency pulse emitted from the inner magnetosphere to trigger magnetic reconnection. By incorporating the wave dynamics of the magnetosphere, we demonstrate how the FRB frequency, the single pulse width, and luminosity are determined by the period, magnetic field, QPO frequency and quake energetics of the magnetar. We find that this model can naturally and self-consistently interpret the X-ray/radio event from SGR 1935+2154 and the QPO in FRB 20191221A. It can also explain the observed wide energy range of repeating FRBs in a narrow bandwidth.

Key words: stars: magnetars – radiation mechanisms: non-thermal – magnetic reconnection

1. Introduction

In recent years, the study of fast radio bursts (FRBs) has been greatly advanced by the progress in the observations. New detections of the galactic events (Bochenek et al. 2020; CHIME/FRB Collaboration et al. 2020), burst polarization (e.g., Michilli et al. 2018; Luo et al. 2020), burst morphology (e.g., Pleunis et al. 2021), source periodicity (e.g., Chime/Frb Collaboration et al. 2020; Pastor-Marazuela et al. 2021; CHIME/FRB Collaboration et al. 2022), source activity (e.g., Li et al. 2021b) and host galaxies (e.g., Bassa et al. 2017; Bhandari et al. 2022), have led to constraints on both progenitor models and radiation mechanisms. However, a complete theoretical understanding of fast radio bursts is still not available and requires more effort (see Zhang 2020b; Xiao et al. 2021, for recent reviews).

Highly magnetized compact objects are usually involved as the central engine of FRBs, such as magnetars, pulsars, and accreting black holes. Among them, the magnetar scenario has been confirmed by the detection of the galactic event (e.g., Bochenek et al. 2020; CHIME/FRB Collaboration et al. 2020; Mereghetti et al. 2020; Li et al. 2021a; Ridnaia et al. 2021; Tavani et al. 2021). Theoretically, the energy resource can come from the internal magnetic energy of magnetars (e.g., Popov & Postnov 2013; Katz 2016; Beloborodov 2017a; Margalit et al. 2020) or the gravitational potential energy when a companion star is involved (e.g., Geng & Huang 2015; Dai et al. 2016; Wang et al. 2016, 2018; Zhang 2020a; Dai 2020; Most & Philippov 2022).

Currently, the mainstream FRB radiation mechanisms can be divided into two categories: the near-field (or close-in) and the far-field (or far-away) model. The near-field model, mainly based on the coherent curvature radiation model near the magnetar surface (e.g., Kumar et al. 2017; Yang & Zhang 2018; Wang et al. 2020a, 2020b; Lu et al. 2020; Yang et al. 2020), can explain the complex temporal behavior of FRBs, while the bunching mechanism for the coherent curvature radiation is unclear. Recently, it is found that magnetospheric radio waves suffer from strong dissipation when the wave becomes nonlinear and cannot escape from the magnetosphere (Beloborodov 2022b; Chen et al. 2022). The far-field model incorporates the synchrotron maser emission at the shock front far from the magnetosphere as the coherent radio emission mechanism (e.g., Lyubarsky 2014; Beloborodov 2017a; Waxman 2017; Margalit & Metzger 2018; Metzger et al. 2019; Plotnikov & Sironi 2019; Beloborodov 2020; Margalit et al. 2020; Wu et al. 2020; Xiao & Dai 2020; Yu et al. 2020). This mechanism has been demonstrated using kinetic plasma simulations (e.g., Plotnikov & Sironi 2019; Sironi et al. 2021). However, it is difficult to explain the sub-second scale quasi-periodic oscillations (QPOs) from FRBs (CHIME/FRB Collaboration et al. 2022; Pastor-Marazuela et al. 2022). It is

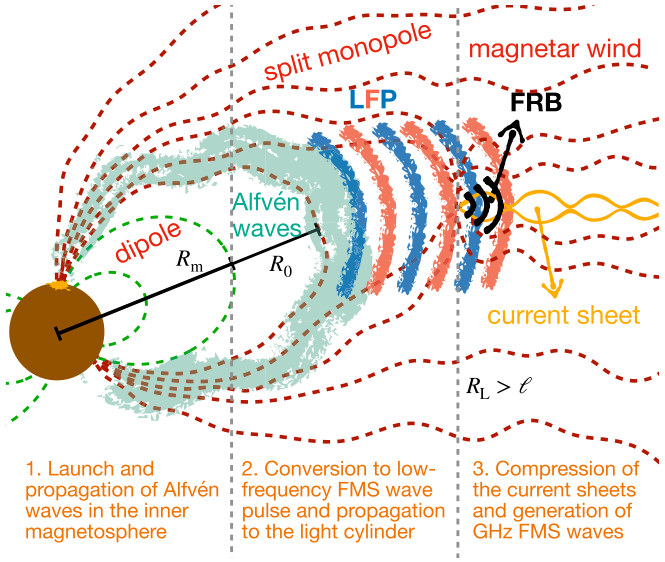

Figure 1. The schematic picture of the intermediate-field FRB model (not to scale). After launch, Alfvén waves propagate along field lines of $R \gtrsim R_0$, and become nonlinear at R_m, which leads to the conversion to an LFP consisting of low-frequency FMS waves. (The Alfvén waves and LFP are drawn with different styles and unrealistic wavelengths to make their presence clear.) The LFP propagates through the light cylinder and compresses the current sheet in the striped magnetar wind. GHz FMS waves are generated by merging islands during the violent magnetic reconnection, which can escape as an FRB.

also found that neither model can fully explain the X-ray/radio event from SGR 1935+2154 (Wang 2020).

Recently, a new type of FRB model is proposed where an FRB is radiated as fast-magnetosonic (FMS) waves generated from violent magnetic reconnection triggered by a low-frequency pulse (LFP) compressing the current sheet (Lyubarsky 2020). As the coherent radio emission is produced near the light cylinder, we refer to it as the "intermediate-field" model. Kinetic plasma simulations (Philippov et al. 2019; Mahlmann et al. 2022) have successfully demonstrated the emission of coherent FMS waves through this mechanism. It is also found that the high linear polarization (Lyubarsky 2020) and the downward frequency drifting (Mahlmann et al. 2022) can be well explained. However, the predicted frequency is significantly lower than the observation of the SGR 1935+2154 event (Wang 2020).

In this paper, we revisit the intermediate-field model and propose that the LFP is produced through nonlinear conversion of Alfvén waves, and propose a toy model for the generation of QPOs. In Section 2, we briefly review the coherent radiation mechanism from magnetic reconnection. In Section 3, we study the injection of energy through Alfvén waves, the wave dynamics in the magnetosphere, and the generation of FRBs and QPOs. In Section 4, we apply our model to observations. The conclusion and discussion are presented in Section 5.

Throughout this paper we adopt the shorthand $X = X_n \times 10^n$ to describe the normalization of quantity X in cgs units.

2. Reconnection Driven Coherent Radio Emission

Magnetic reconnection is a process of changing the magnetic topology when two oppositely directed magnetic field lines approach each other forming a current sheet at the center. The onset of magnetic reconnection is triggered when the current sheet becomes tearing or kink unstable and breaks into a self-similar chain of plasmoids extending down to the kinetic scale (Uzdensky et al. 2010). Fast magnetic reconnection proceeds when the plasmoids collide and merge into larger islands. During the coalescence of plasmoids, magnetic energy is dissipated and FMS waves are produced. In highly magnetized systems with magnetization parameter $\sigma \equiv B^2/4\pi\rho c^2 \gg 1$, FMS waves have a similar dispersion relation as vacuum electromagnetic waves (Thompson & Blaes 1998; Li et al. 2019) and can convert to coherent radio waves (e.g., Lyubarsky 2019; Philippov et al. 2019; Lyubarsky 2020).

It has been proposed that the coherent emission of FRBs are GHz FMS waves generated by the plasmoid collision during magnetic reconnection (Lyubarsky 2020). In their picture, the current sheets in the magnetar wind are compressed by an external outgoing LFP and become tearing unstable under the perturbation, and magnetic reconnection is initiated. Coherent FMS waves are produced in the reconnection and can escape as fast radio bursts. Kinetic simulations have confirmed this process and found that FMS waves takes only a small fraction of the reconnection energy (Mahlmann et al. 2022).

The characteristic frequency of the coherent FMS waves is determined by the size of the plasmoid λ'_c. Note we use the primed symbols to mark parameters measured in the co-moving frame of the plasma throughout the paper. In the plasma comoving frame, $\omega'_c \approx c/\lambda'_c$. The typical plasmoid size is found to be proportional to the width of the current sheet $\lambda'_c = \varsigma a'$ with $\varsigma \sim 10$–100 (Philippov et al. 2019; Lyubarsky 2020), and the width depends on the Larmor radius $a' = \varpi r_L$ with ϖ being a few.

The plasmoid size can be obtained by balancing the pressure and energy (Lyubarsky 2020),

$$\lambda'_c = \sqrt{\frac{8\pi\beta_{\rm rec}\varpi}{e\sigma_T}}\frac{m_e c^2}{B'^{3/2}}, \quad (1)$$

where σ_T is the Thomson scattering cross section, $\beta_{\rm rec} \sim 0.1$ is the reconnection rate, $B' = B/\Gamma$ is the magnetic field in the comoving frame and Γ is the bulk Lorentz factor. Therefore, the characteristic frequency in the observer's frame is,

$$\nu_c \equiv \Gamma\omega'_c/2\pi \approx 2.1\eta_1^{-1}\Gamma^{-1/2}B_8^{3/2}\ {\rm GHz}, \quad (2)$$

where $\eta \equiv \varsigma\varpi^{1/2}\beta_{\rm rec}^{1/2}$. This expression is confirmed numerically but with a slightly different expression of η (Mahlmann et al. 2022).

3. Intermediate-field FRB Models and QPOs

Our model is illustrated in Figure 1, which describes how an FRB is produced from a magnetar quake: (1) Alfvén waves are generated by magnetar quakes, which propagates in the inner magnetosphere. (2) When the wave amplitudes becomes comparable to the background magnetic field, Alfvén waves can convert to FMS waves with the same wave frequency. The low-frequency FMS waves compose an LFP and propagates into the striped wind. (3) The LFP compresses the current sheets in the striped wind and initiate violent magnetic reconnection, which can generate GHz FMS waves. (4) Current sheets are also build up behind the LFP, which can generate high-frequency FMS waves but suffers strong dissipation. In the following subsections, we discuss these four points in details respectively.

3.1. Launch and Propagation of Alfvén Waves in the Inner Magnetosphere

For a magnetar with a surface dipole magnetic field B_d and radius $R_* \approx 10^6$ cm, the total magnetic energy is $E_B = B_d^2 R_*^3/6 \approx 1.7 \times 10^{47} B_{d,15}^2$ erg. The internal magnetic field B_* can be higher and we parameterize it by $B_* = \zeta B_d$ with $\zeta > 1$. The internal magnetic energy can be released by a sudden starquake and crustal motion which are accompanied by the crustal shear oscillations (e.g., Thompson & Duncan 1995; Duncan 1998; Thompson & Duncan 2001). Such oscillations are proposed to explain the QPOs observed in magnetar X-ray flares (e.g., Israel et al. 2005; Strohmayer & Watts 2005, 2006).

The oscillation frequency depends on the magnetar properties. It has been found that the wave frequency of the toroidal shear modes with the lowest radial node (symbolized by $_l t_0$) follows $f_A(_l t_0) \approx 12.2 l^{1/2}(l+1)^{1/2}$ Hz with $l \geqslant 2$ being an integer in the magnetar crust (Duncan 1998). Later it is found that the crustal shear modes will couple with the MHD modes of the magnetar core, and the frequency and duration of the oscillation will be modified (e.g., Levin 2007; van Hoven & Levin 2012; Gabler et al. 2016). Such theories predict that the fundamental frequency of magnetar QPOs can be as low as $f_A \sim \mathcal{O}(1)$ Hz, and it can be much higher for high order overtones, even up to $f_A \sim \mathcal{O}(10^3)$ Hz (e.g., van Hoven & Levin 2012). The power spectrum of QPOs is found to be dominated by several frequencies depending on the magnetar properties, e.g., Figure 9 in van Hoven & Levin (2012), which is in general consistent with observations such as Figure 3 in Israel et al. (2005).

As the shear wave propagates in the crust, it shakes the anchored magnetic field lines, and launches Alfvén waves into the magnetosphere (Thompson & Duncan 2001; Li et al. 2016; Thompson et al. 2017; Bransgrove et al. 2020). The Alfvén waves carry energy into the magnetosphere and propagate along the field lines. The field-line equation is $r = R\sin^2\theta$, where R is the maximum distance of the field line to the magnetar center and θ is the angle to the magnetic axis. For field lines with $R \gg R_*$, the field-line length is $l \simeq \pi R/2$.

The generated Alfvén waves of frequency $f_A \sim 1$–10^3 Hz in the magnetosphere can propagate along field lines with $l \geqslant l_0 = \pi R_0/2 = c/f_A = 1.9 \times 10^{10} f_A^{-1}$ cm as a perturbation. Note that Alfvén waves traveling on field lines with $l < l_0$ may suffer from strong nonlinear interactions and the dissipation mechanism is unclear. Thus we only consider magnetar quakes occurred near the magnetic polar region, so that magnetar oscillations can launch Alfvén waves into the magnetosphere before damping (e.g., Levin 2007; van Hoven & Levin 2012).

We consider a sudden release of internal magnetic energy of $E_q = h\mathrm{SB}_*^2/8\pi$ in the crust with a crust thickness $h \approx 10^5$ cm and an area S_q. Note in the quake region, the internal magnetic energy can be much larger than the surface field with $B_*/B_d = \zeta \gg 1$. The magnetar quake can simultaneously launch a number of waves with different frequencies, that are of different damping timescales (e.g., Levin 2007; van Hoven & Levin 2012; Gabler et al. 2016). We consider that the Alfvén wave of frequency f_A is the dominated one which carries most of the energy, and a number (n_A) of waves at this frequency has been excited. The energy carried by each wave is parameterized as $\epsilon E_q \approx L_A/f_A$ with a power L_A and $\epsilon < 1/n_A$. The wave is launched from the magnetar surface within the same area,

$$S_q = 2.5 \times 10^8 L_{A,44} f_{A,2}^{-1} B_{d,15}^{-2} \epsilon^{-1} \zeta^{-2} \ \mathrm{cm}^2. \quad (3)$$

The corresponding wave amplitude in the magnetosphere is $\delta B = \sqrt{8\pi L_A/S_q c}$. Its relative amplitude to the background field near the magnetar surface is

$$\frac{\delta B}{B_d} \approx 0.02 f_{A,2}^{1/2} \epsilon^{1/2} \zeta, \quad (4)$$

3.2. Conversion to an LFP and its Propagation in the Outer Magnetosphere

As the Alfvén wave propagates in the magnetosphere, its amplitude grows as $\delta B/B_d \propto r^{3/2}$ (e.g., Kumar & Bošnjak 2020; Yuan et al. 2020). When the relative amplitude grows to $\delta B/B \approx 1$ (Yuan et al. 2020, 2022) at a distance of

$$R_\mathrm{m} \approx 1.4 \times 10^7 f_{A,2}^{-1/3} \epsilon^{-1/3} \zeta^{-2/3} \ \mathrm{cm}, \quad (5)$$

the Alfvén waves will become nonlinear and shear the magnetosphere. The background magnetic field here can be estimated from a dipole $B_\mathrm{m} = B_* R_*^3 R_\mathrm{m}^{-3}$. Under the strong shear, the magnetosphere becomes unstable. A large part of the Alfvén waves will be converted to FMS waves that propagates outwards radially in the form of an LFP (Li et al. 2019, 2021c; Yuan et al. 2021) due to the interaction with the curved magnetic field line. The remaining Alfvén waves will dissipate inside the magnetosphere by nonlinear instabilities (Yuan et al. 2020) or absorbed by the magnetar (Li & Beloborodov 2015).

We here mainly consider the LFP, which can carry a large portion of the energy of Alfvén waves (Yuan et al. 2022). The LFP is made up of low-frequency FMS waves converted from the propagating Alfvén waves. This process can be viewed as the nonlinear interaction between Alfvén waves and the curved background magnetic field. The leading order wave interaction can be treated as three-wave interaction with

$$\boldsymbol{k}_A + \boldsymbol{k}_{\rm bg} = \boldsymbol{k}_{\rm LFP}, \ \text{and}\, f_{\rm LFP} = f_A, \tag{6}$$

where $\boldsymbol{k}$ is the wavenumber and $\boldsymbol{k}_{\rm bg}$ is the wavenumber of the background magnetic field (Yuan et al. 2021). Notably in this process the generated low-frequency FMS wave will have the same frequency as the Alfvén wave, as the background field does not have a time component, i.e., $f_{\rm bg} = 0$. The LFP will propagate outward radially with its thickness conserved as found by numerical simulations (Yuan et al. 2022). Therefore the LFP keeps its wave frequency when propagating.

During the propagation of the LFP at $r > R_{\rm m}$, its toroidal field follows $rB_{\rm LFP} = B_{\rm LFP,\ m} R_{\rm m}$ with $B_{\rm LFP,\ m} \approx B_{\rm m}$ (Parfrey et al. 2013; Yuan et al. 2020, 2022). As the energy contained in the LFP is higher than that of background field, the magnetosphere is distorted. The poloidal field follows $r^2 B_p = B_{\rm m} R_{\rm m}^2$ from the conservation of magnetic flux. Thus the magnetosphere at $R > R_{\rm m}$ can be treated as a split monopole. When the LFP reaches the light cylinder at $R_L = cP/2\pi$, where P is the magnetar rotation period, its toroidal field and the poloidal field of the magnetosphere are given by

$$B_{\rm LFP,L} = 3.4 \times 10^8 B_{d,15} f_{A,2}^{2/3} \epsilon^{2/3} \zeta^{4/3} \left(\frac{P}{3\ {\rm s}}\right)^{-1} {\rm G}; \tag{7}$$

$$B_{p,m}(R_{\rm L}) = 3.4 \times 10^5 B_{d,15} f_{A,2}^{1/3} \epsilon^{1/3} \zeta^{2/3} \left(\frac{P}{3\ {\rm s}}\right)^{-2} {\rm G}. \tag{8}$$

When propagating in the magnetosphere, the FMS waves also suffer from nonlinear steepening when the wave amplitude is comparable to the background magnetic field, and form shocks (Lyubarsky 2020; Beloborodov 2022a, 2022b; Chen et al. 2022). Considering the nonlinear steepening caused by the variation of wave velocity across the wavelength, which depends on the local density and magnetic field (Lyubarsky 2020), the shock formation distance is

$$R_{\rm stp} \sim \sigma_{\rm LFP} \Gamma^2 c / f_A = 3 \times 10^{10} \Gamma_1^2 \sigma_{\rm LFP}\ {\rm cm}, \tag{9}$$

where the plasma bulk Lorentz factor for the LFP in the magnetosphere could be mild relativistic $\Gamma \sim 10$. Thus as long as the magnetization of the LFP is $\sigma_{\rm LFP} \gg 1$, the shock formation distance is outside the light cylinder for magnetars. However, the effect of high electric field may still be able to dissipate a fraction of LFP energy (Beloborodov 2022a), which is not considered here.

3.3. Generation of FRBs and QPOs in the Compressed Current Sheets in the Striped Wind

The LFP will eventually enter the striped wind and accelerates the plasma to a bulk Lorentz factor of $\Gamma \approx 0.5\sqrt{B_{\rm LFP,\ L}/B_{\rm w}(R_{\rm L})}$ by compressing it, where the wind field is described as a monopole with $B_{\rm w}(r) = B_p(R_L) R_L / r$ and $B_p(R_L)$ is the poloidal field of the magnetosphere at the light cylinder. The pulse front propagates into the magnetar wind launched by the unperturbed magnetosphere with $B_p(R_L) = B_* R_*^3 R_{\rm L}^{-3}$. However, the energy carried by the LFP amplifies the magnetic field at the light cylinder to $B_{p,m}(R_{\rm L})$, which further enhances the toroidal magnetic field in the striped wind to $B_{\rm w}(R_{\rm L}) \sim B_{p,m}(R_{\rm L})$. Therefore, the rear part of LFP will interact with the current sheets in the striped wind launched by the perturbed magnetosphere (see Figure 1). In reality, the amplification of the wind toroidal field and the formation of the current sheet are highly dynamic, we therefore expect the wind field to be in the range $B_{\rm w}(R_{\rm L}) \in [B_* R_*^3 R_{\rm L}^{-3},\ B_{p,m}(R_{\rm L})]$.

The corresponding maximum and minimum Lorentz factors of the accelerated LFPs are then

$$\Gamma^{\rm max} = 496 \epsilon^{1/3} \zeta^{2/3} f_{A,2}^{1/3} \left(\frac{P}{3\ {\rm s}}\right);$$
$$\Gamma^{\rm min} = 16 \epsilon^{1/6} \zeta^{1/3} f_{A,2}^{1/6} \left(\frac{P}{3\ {\rm s}}\right)^{1/2}. \tag{10}$$

In the following we parameterize $\Gamma = 100\Gamma_2$ which lies between $\Gamma^{\rm min}$ and $\Gamma^{\rm max}$. We expect $\Gamma \to \Gamma^{\rm min}$ for LFPs consisting of multiple waves (e.g., $n_A \gtrsim 3$), such as in the SGR $1935+2154$ event and FRB 20191221A (see Section 4 for more details).

Magnetic reconnection will be triggered when the LFP compresses the current sheet in the striped wind, which leads to the generation of high-frequency FMS waves as discussed in Section 2. Substituting $B_{\rm LFP,L}$ and Γ into Equation (2), we obtain the frequency of the FMS waves,

$$\nu_{\rm c} = 1.3 f_{A,2} B_{d,15}^{3/2} \epsilon \zeta^2 \left(\frac{P}{3\ {\rm s}}\right)^{-3/2} \eta_1^{-1} \Gamma_2^{-1/2}\ {\rm GHz}, \tag{11}$$

which lies in the radio band.

The overall energy dissipation in the magnetic reconnection will be mediated by the wave frequency of LFP, which is identical to the Alfvén wave frequency (Equation (6)). In this case, we expect

$$f_{\rm FRB} \sim f_{\rm LFP} = f_A, \tag{12}$$

which makes the observed QPO signals in some FRBs. Note in this expression, we assume $f_A > 1/P$, which will in general be satisfied for magnetars with $P \gtrsim 0.1$ s. Otherwise the FRB profile will also be modulated by the spin period.

As the plasma is accelerated to a bulk Lorentz factor of Γ, the observed width of one single pulse and peak luminosity will

be

$$W_{\rm p} \approx 1/(\Gamma f_A), \tag{13}$$

$$L_{\rm FMS} \approx \kappa \Gamma^2 L_A. \tag{14}$$

The produced FMS waves suffers from nonlinear wave interactions, and it can escape only when its optical depth $\tau_{\rm NL} \lesssim 10$ (Lyubarsky 2020), which is given by

$$\tau_{\rm NL} \sim \frac{\kappa 2\pi \nu R_{\rm L}}{2\Gamma^2 c} = 0.5 \kappa_{-5.5} \nu_{\rm c,9} \left(\frac{P}{3\ {\rm s}}\right) \Gamma_2^{-2}, \tag{15}$$

where $\kappa = B^2_{\rm FMS}/B^2_{\rm LFP,\ L}$ is the energy ratio of the high-frequency FMS waves to the LFP. In 2D simulations, it is found that a fraction $\kappa \sim 10^{-4}$ of energy from the LFP is converted to the FMS, interpreted as an upper limit of the efficiency (Mahlmann et al. 2022). The ratio of radio to X-ray energy of FRB200428 is found to be 10^{-6}–10^{-5} (Ridnaia et al. 2021). Here we take $\kappa \sim 10^{-5.5}$ to be the fiducial value. Therefore, the FMS waves generated at the light cylinder can escape without significant dissipation and be observed as FRBs.

3.4. The Current Sheets Behind the LFP

There are also current sheets behind the LFP inside the magnetosphere, which has been suggested to produce an FRB (Wang 2020; Yuan et al. 2020, 2022). The reconnected fields are the poloidal component (Yuan et al. 2022), and the frequency of FMS waves produced in those current sheets is

$$\nu = 4.0 \times 10^{14} B_{d,15}^{3/2} f_A^{1/2} \zeta \Gamma_{\rm pl} \epsilon^{1/2} (R_{\rm m}/R)^3 \eta_1^{-1}\ {\rm Hz}, \tag{16}$$

where the plasmoid bulk Lorentz factor inside the magnetosphere can be a few, $\Gamma_{\rm pl} \sim 1$–10. The FMS wave frequency ranges from optical to radio for $R \in (R_{\rm m}, R_{\rm L})$ for the current sheet inside the magnetosphere.

However, the FMS waves emitted deep inside the magnetosphere at $R \sim R_{\rm m}$ also suffers from strong dissipation of the nonlinear wave interactions. The optical depth inside the magnetosphere is $\tau_{\rm NL} \approx (B_{\rm FMS}/B_p)^2 \omega R/c$ (see Equation (A3) in Lyubarsky 2020) with the FMS wave magnetic field $B_{\rm FMS} = \sqrt{2L_{\rm FMS}/r^2}$ and B_p being treated as a monopole. Setting $\tau_{\rm NL} \sim 10$, we obtain a mean-free-path

$$\ell \sim 3.4 \times 10^6 B_{d,15}^{1/2} f_{A,2}^{1/6} \epsilon^{1/6} \zeta^{1/3} \nu_{14}^{-1/4} L_{\rm FMS,42}^{-1/4}\ {\rm cm}, \tag{17}$$

which is much smaller than R_L for a typical magnetar with period 0.1–10 s. Therefore, such optical radiation will be dissipated inside the magnetosphere.

The frequency of the FMS waves produced by the current sheet behind the LFP at larger radii ($R \sim R_L$) could lie in the radio band. However, as the magnetic reconnection is supported by the reversed poloidal magnetic field, the magnetic flux is much smaller at near the light cylinder,

$$\frac{B^2_{p,m}(R_{\rm L})}{B^2_{\rm LFP,\ L}} = 1.0 \times 10^{-6} f_{A,2}^{-2/3} \epsilon^{-2/3} \zeta^{-4/3} \left(\frac{P}{3\ {\rm s}}\right)^{-2}. \tag{18}$$

Therefore, the FMS waves produced behind the LFP cannot be the primary source of FRB, as its available magnetic energy here is much smaller than the energy of the LFP.

4. Application to the Observed QPOs of FRBs and the SGR 1935+2154 Event

We now apply our model to the observed QPOs in the X-ray/radio burst of SGR 1935+2154 and in other FRBs. Observations show that the FRB from the galactic magnetar, SGR 1935+2154 (Bochenek et al. 2020; CHIME/FRB Collaboration et al. 2020), is associated with a hard X-ray burst by several X-ray instruments (Mereghetti et al. 2020; Li et al. 2021a; Ridnaia et al. 2021; Tavani et al. 2021). This magnetar is of spin period and surface magnetic field $P = 3.2$ s and $B_* = 2.2 \times 10^{14}$ G, respectively (Olausen & Kaspi 2014; Israel et al. 2016). Two radio pulses separated by 30 ms are found in this FRB, while more pulses are detected in X-ray bands. The reason may be that the opening angle of the radio emission is much smaller than that of the X-ray emission (e.g., Wang 2020). Especially, a QPO of $f_A \approx 40$ Hz and $n_A \gtrsim 8$ is detected in the X-ray light curve by the Insight-HXMT (Li et al. 2022). The observed pulse width is 0.3–0.6 ms by CHIME and STARE2 in 0.6–1.3 GHz (Bochenek et al. 2020; CHIME/FRB Collaboration et al. 2020). Substituting $\epsilon < 1/n_A \sim 1/8$, $W_{\rm p} \sim 0.5$ ms, and $\nu_{\rm c} \sim 1$ GHz as well as the observed radio peak luminosity $L_{\rm FMS} \approx 10^{38}$ erg s^{-1} (Bochenek et al. 2020; Zhou et al. 2020) into Equations (11) (13) and (14), we obtain $\Gamma \sim 50$, $\zeta \gtrsim 3.5\eta_1^{1/2}$ and $L_A \approx 1.4 \times 10^{40} \kappa_{-5.5}^{-1}$ erg s^{-1}. The required Γ is in the allowed range $[22\eta_1^{1/6}, 977\eta_1^{1/3}]$ from Equation (10), which is close to $\Gamma^{\rm min}$ as we expected, and the required L_A is comparable to the observed X-ray luminosity, 10^{40} erg s^{-1} (Mereghetti et al. 2020; Li et al. 2021a). Therefore, our model can explain this event self-consistently.

QPO signals are also observed in individual FRB events, such as the 4.6 Hz QPO in FRB 20191221A, 357.1 Hz in FRB 20210206A, 93.4 Hz in FRB 20210213A detected by CHIME (CHIME/FRB Collaboration et al. 2022), and the 2.4 kHz QPO in FRB 20201020A detected by Apertif (Pastor-Marazuela et al. 2022). It has been suggested that the 4.6 Hz QPO may be caused by the magnetar spin period (Beniamini & Kumar 2022), however, such a spin-period scenario will be difficult to explain the high-frequency QPOs, especially the 2.4 kHz one (Pastor-Marazuela et al. 2022). While the magnetar oscillation can offer a natural explanation. The observed QPOs with frequencies larger than 93.4 Hz mentioned above can be explained by the overtones in a wide parameter range. While the 4.6 Hz QPO in FRB 20191221A may relate to

the fundamental mode. We here focus on this source, which has the highest significance (CHIME/FRB Collaboration et al. 2022). The observed radio frequency, single pulse width, and QPO frequency of FRB 20191221A are $\nu_c \approx 0.7$ GHz, $W_p \approx 4$ ms, and $f_A \approx 4.6$ Hz with $n_A \approx 9$, respectively. The total duration of this event is $\sim$3 s and we would expect $P > 3$ s so that the QPO signal is not contaminated by the magnetar rotation. Substituting them into Equations (11) and (13), we obtain $\Gamma \approx 54$ and $\zeta \gtrsim 9\eta_1^{1/2}(P/3\ \mathrm{s})^{3/4}B_{d,15}^{-3/4}$. The required Γ is in the allowed range $[14\eta_1^{1/6}(P/3\ \mathrm{s})^{3/4}B_{d,15}^{-1/4},\ 367\eta_1^{1/3}(P/3\ \mathrm{s})^{3/2}B_{d,15}^{-1/2}]$ and we find again that the derived bulk Lorentz factor is close to $\Gamma^{\min}$. Thus the QPO in FRB 20191221A can also be explained by our model.

5. Conclusion and Discussion

In this paper, we generalized the wave dynamics in the magnetosphere from the previous simulation results in Yuan et al. (2020, 2022) and applied it in the intermediate-field FRB model. We focused on the recently observed QPOs in some FRBs and found that it can be self-consistently explained in the revised model. The launch of Alfvén waves into the magnetosphere generates an LFP, which is made up of FMS waves at approximately the same frequencies of Alfvén waves (f_A). This further generates FRBs when the LFP dissipates its energy at the current sheet near the light cylinder. The FRB light curve is thus modulated by the frequency of the LFP, exhibiting QPOs at a frequency $\sim f_A$. The major difference of our calculations from Lyubarsky (2020) is the treatment of magnetic field configurations of the LFP and the magnetar wind, as we considered the wave dynamics in the magnetosphere.

The FRB frequency (Equation (11)), the single pulse width (Equation (13)), and luminosity (Equation (14)) mainly depend on the magnetar's period and magnetic field and the quake energetics and QPO frequency. With physically reasonable values for the parameters, we find that this model can naturally and self-consistently interpret the observed frequency, pulse width, luminosity and QPO signal of the radio/X-ray event from SGR 1935+2154 and FRB 20191221A.

Our model can also naturally explain the observed wide energy span detected in a relative narrow frequency band, such as the broad energy range (4×10^{36}–8×10^{39} erg) observed in FRB 121102 at 1.25 GHz (Li et al. 2021b), as the frequency does not depend on the flare energy apparently. In certain parameter space for young magnetars, the frequency is in the optical band, indicating the possibility of producing fast optical transients.

In general, QPOs will modulate the FRB light curve. Direct identification of QPOs may require at least around ten individual pulses ($n_A \gtrsim 10$) in one event (e.g., CHIME/FRB Collaboration et al. 2022). For the high-frequency QPOs ($f_A \gtrsim 1$ kHz), the corresponding FRB pulses may overlap with each other, making it difficult to identify from the data. While for the low-frequency QPOs ($f_A \sim 10$ Hz), one may only expect to detect them from magnetars with $P \gtrsim 10/f_A \sim 1$ s so that the QPO signal is not contaminated by the magnetar spin. Besides, the small opening angles of FRBs caused by the relativistic beaming effect also make it challenging to detect multiple pulses in a single event. Thus, direct detection of QPOs will only be possible for some rare events. However, for repeating FRBs, QPOs would affect the waiting time distribution even if only several pulses are presented in the observed individual events. The peak at 3.4 ms in the waiting time distribution of FRB 121102 may be such a case (Li et al. 2021b). Another possibility is to detect QPOs from the counterparts of FRBs, such as the non-thermal X-ray burst in SGR 1935+2154, although the radiation mechanism in X-ray QPOs requires further detailed studies.

As only a small portion of energy is dissipated to power FRBs, the majority of the energy will be dissipated into X-rays or carried by the ejecta. The ejecta would further power an afterglow or a nebula (e.g., Beloborodov 2017a; Waxman 2017; Margalit & Metzger 2018; Wang & Lai 2020). As magnetar flares may eject a large fraction of mass (e.g., Granot et al. 2006), high-energy cosmic rays can also be produced in such afterglows/nebulae. Besides, such a magnetic reconnection process could also take place in neutron star mergers (e.g., Wang et al. 2018; Most & Philippov 2022) and accreting black holes (e.g., Beloborodov 2017b; Sridhar et al. 2021), thus we might also expect such reconnection driven transients from neutron star mergers, X-ray binaries, or active galactic nuclei.

Acknowledgments

We thank the referee for helpful comments. J.S.W. thanks J. Kirk, B. Reville, and F. Guo for discussions. J.S.W. acknowledges the support from the Alexander von Humboldt Foundation. X.L. is supported by NSERC, funding reference #CITA 490888–16 and the Jeffrey L. Bishop Fellowship. Research at Perimeter Institute is supported in part by the Government of Canada through the Department of Innovation, Science and Economic Development Canada and the Province of Ontario through the Ministry of Colleges and Universities. Z.G.D. is supported by the National Key Research and Development Program of China (Grant No. 2017YFA0402600), the National SKA Program of China (Grant No. 2020SKA0120300), and the National Natural Science Foundation of China (Grant No. 11833003). X.F.W. is supported by the National Natural Science Foundation of China (Grant Nos. 11725314, 12041306) and the National SKA Program of China (2022SKA0130101).

References

Bassa, C. G., Tendulkar, S. P., Adams, E. A. K., et al. 2017, ApJL, 843, L8
Beloborodov, A. M. 2017a, ApJL, 843, L26
Beloborodov, A. M. 2017b, ApJ, 850, 141
Beloborodov, A. M. 2020, ApJ, 896, 142
Beloborodov, A. M. 2022a, arXiv:2210.13509

Beloborodov, A. M. 2022b, PhRvL, 128, 255003
Beniamini, P., & Kumar, P. 2022, arXiv:2211.07669
Bhandari, S., Heintz, K. E., Aggarwal, K., et al. 2022, AJ, 163, 69
Bochenek, C. D., Ravi, V., Belov, K. V., et al. 2020, Natur, 587, 59
Bransgrove, A., Beloborodov, A. M., & Levin, Y. 2020, ApJ, 897, 173
CHIME/FRB Collaboration, Amiri, M., Andersen, B. C., et al. 2020, Natur, 582, 351
CHIME/FRB Collaboration, Andersen, B. C., Bandura, K., et al. 2022, Natur, 607, 256
CHIME/FRB Collaboration, Andersen, B. C., Bandura, K. M., et al. 2020, Natur, 587, 54
Chen, A. Y., Yuan, Y., Li, X., & Mahlmann, J. F. 2022, arXiv:2210.13506
Dai, Z. G. 2020, ApJL, 897, L40
Dai, Z. G., Wang, J. S., Wu, X. F., & Huang, Y. F. 2016, ApJ, 829, 27
Duncan, R. C. 1998, ApJL, 498, L45
Gabler, M., Cerdá-Durán, P., Stergioulas, N., Font, J. A., & Müller, E. 2016, MNRAS, 460, 4242
Geng, J. J., & Huang, Y. F. 2015, ApJ, 809, 24
Granot, J., Ramirez-Ruiz, E., Taylor, G. B., et al. 2006, ApJ, 638, 391
Israel, G. L., Belloni, T., Stella, L., et al. 2005, ApJL, 628, L53
Israel, G. L., Esposito, P., Rea, N., et al. 2016, MNRAS, 457, 3448
Katz, J. I. 2016, ApJ, 826, 226
Kumar, P., & Bošnjak, Ž 2020, MNRAS, 494, 2385
Kumar, P., Lu, W., & Bhattacharya, M. 2017, MNRAS, 468, 2726
Levin, Y. 2007, MNRAS, 377, 159
Li, C. K., Lin, L., Xiong, S. L., et al. 2021a, NatAs, 5, 378
Li, D., Wang, P., Zhu, W. W., et al. 2021b, Natur, 598, 267
Li, X., & Beloborodov, A. M. 2015, ApJ, 815, 25
Li, X., Beloborodov, A. M., & Sironi, L. 2021c, ApJ, 915, 101
Li, X., Ge, M., Lin, L., et al. 2022, ApJ, 931, 56
Li, X., Levin, Y., & Beloborodov, A. M. 2016, ApJ, 833, 189
Li, X., Zrake, J., & Beloborodov, A. M. 2019, ApJ, 881, 13
Lu, W., Kumar, P., & Zhang, B. 2020, MNRAS, 498, 1397
Luo, R., Wang, B. J., Men, Y. P., et al. 2020, Natur, 586, 693
Lyubarsky, Y. 2014, MNRAS, 442, L9
Lyubarsky, Y. 2019, MNRAS, 483, 1731
Lyubarsky, Y. 2020, ApJ, 897, 1
Mahlmann, J. F., Philippov, A. A., Levinson, A., Spitkovsky, A., & Hakobyan, H. 2022, ApJL, 932, L20
Margalit, B., Beniamini, P., Sridhar, N., & Metzger, B. D. 2020, ApJL, 899, L27
Margalit, B., & Metzger, B. D. 2018, ApJL, 868, L4
Mereghetti, S., Savchenko, V., Ferrigno, C., et al. 2020, ApJL, 898, L29
Metzger, B. D., Margalit, B., & Sironi, L. 2019, MNRAS, 485, 4091
Michilli, D., Seymour, A., Hessels, J. W. T., et al. 2018, Natur, 553, 182
Most, E. R., & Philippov, A. A. 2022, MNRAS, 515, 2710
Olausen, S. A., & Kaspi, V. M. 2014, ApJS, 212, 6
Parfrey, K., Beloborodov, A. M., & Hui, L. 2013, ApJ, 774, 92
Pastor-Marazuela, I., Connor, L., van Leeuwen, J., et al. 2021, Natur, 596, 505
Pastor-Marazuela, I., van Leeuwen, J., Bilous, A., et al. 2022, arXiv:2202.08002
Philippov, A., Uzdensky, D. A., Spitkovsky, A., & Cerutti, B. 2019, ApJL, 876, L6
Pleunis, Z., Good, D. C., Kaspi, V. M., et al. 2021, ApJ, 923, 1
Plotnikov, I., & Sironi, L. 2019, arXiv:1901.01029
Popov, S. B., & Postnov, K. A. 2013, arXiv:1307.4924
Ridnaia, A., Svinkin, D., Frederiks, D., et al. 2021, NatAs, 5, 372
Sironi, L., Plotnikov, I., Nättilä, J., & Beloborodov, A. M. 2021, PhRvL, 127, 035101
Sridhar, N., Sironi, L., & Beloborodov, A. M. 2021, MNRAS, 507, 5625
Strohmayer, T. E., & Watts, A. L. 2005, ApJL, 632, L111
Strohmayer, T. E., & Watts, A. L. 2006, ApJ, 653, 593
Tavani, M., Casentini, C., Ursi, A., et al. 2021, NatAs, 5, 401
Thompson, C., & Blaes, O. 1998, PhRvD, 57, 3219
Thompson, C., & Duncan, R. C. 1995, MNRAS, 275, 255
Thompson, C., & Duncan, R. C. 2001, ApJ, 561, 980
Thompson, C., Yang, H., & Ortiz, N. 2017, ApJ, 841, 54
Uzdensky, D. A., Loureiro, N. F., & Schekochihin, A. A. 2010, PhRvL, 105, 235002
van Hoven, M., & Levin, Y. 2012, MNRAS, 420, 3035
Wang, F. Y., Wang, Y. Y., Yang, Y.-P., et al. 2020a, ApJ, 891, 72
Wang, W.-Y., Xu, R., & Chen, X. 2020b, ApJ, 899, 109
Wang, J.-S. 2020, ApJ, 900, 172
Wang, J.-S., & Lai, D. 2020, ApJ, 892, 135
Wang, J.-S., Peng, F.-K., Wu, K., & Dai, Z.-G. 2018, ApJ, 868, 19
Wang, J.-S., Yang, Y.-P., Wu, X.-F., Dai, Z.-G., & Wang, F.-Y. 2016, ApJ, 822, L7
Waxman, E. 2017, ApJ, 842, 34
Wu, Q., Zhang, G. Q., Wang, F. Y., & Dai, Z. G. 2020, ApJL, 900, L26
Xiao, D., & Dai, Z.-G. 2020, ApJL, 904, L5
Xiao, D., Wang, F., & Dai, Z. 2021, SCPMA, 64, 249501
Yang, Y.-P., & Zhang, B. 2018, ApJ, 868, 31
Yang, Y.-P., Zhu, J.-P., Zhang, B., & Wu, X.-F. 2020, ApJL, 901, L13
Yu, Y.-W., Zou, Y.-C., Dai, Z.-G., & Yu, W.-F. 2020, arXiv:2006.00484
Yuan, Y., Beloborodov, A. M., Chen, A. Y., et al. 2022, ApJ, 933, 174
Yuan, Y., Beloborodov, A. M., Chen, A. Y., & Levin, Y. 2020, ApJL, 900, L21
Yuan, Y., Levin, Y., Bransgrove, A., & Philippov, A. 2021, ApJ, 908, 176
Zhang, B. 2020a, ApJL, 890, L24
Zhang, B. 2020b, Natur, 587, 45
Zhou, P., Zhou, X., Chen, Y., et al. 2020, ApJ, 905, 99